Modulation of flow over low-order topographies by low-order roughness

Shyuan Cheng,[1] Ali M. Hamed,[2] Matias Colombo,[3] and Leonardo P. Chamorro[3,4,5,6,*]
[1]*Department of Mechanical Engineering, University of South Carolina, Columbia, South Carolina 29209, USA*
[2]*Department of Mechanical Engineering, Union College, Schenectady, New York 12308, USA*
[3]*Department of Mechanical Science and Engineering, University of Illinois, Urbana, Illinois 61801, USA*
[4]*Department of Civil and Environmental Engineering, University of Illinois, Urbana, Illinois 61801, USA*
[5]*Department of Aerospace Engineering, University of Illinois, Urbana, Illinois 61801, USA*
[6]*Department of Earth Science & Environmental Change, University of Illinois, Urbana, Illinois 61801, USA*

(Received 5 November 2025; accepted 28 May 2026; published 15 June 2026)

The interaction between low-order roughness and large-scale topography is experimentally investigated using high-resolution particle image velocimetry in a refractive-index-matched channel at two bulk Reynolds numbers differing by an order of magnitude, $\mathrm{Re} = 4.0 \times 10^3$ and 4.0×10^4. A two-dimensional sinusoidal roughness is superimposed on a two-dimensional wavy wall to isolate the effects of multiscale surface modulation on near-wall turbulence. The added roughness reorganizes the flow by inducing larger coherent structures near the surface. Two-point correlations and integral length scales confirm enhanced near-wall coherence, while quadrant-hole analysis reveals a marked suppression of ejection events. This suppression weakens the local turbulence production term $-\langle u'v'\rangle dU/dy$, leading to attenuation of the separated shear layer that develops downstream from the topographic crest within the adverse-pressure-gradient region. The resulting flow exhibits up to 25% lower peak turbulent kinetic energy and Reynolds shear stress relative to the smooth-wavy configuration. Even modest low-order roughness can therefore reorganize the coupling between near-wall and outer-layer motions, a mechanism that persists across an order of magnitude in Reynolds number and offers valuable insight for modeling transport and drag over natural and engineered surfaces.

DOI: 10.1103/nrd5-ny95

I. INTRODUCTION

Characterizing the flow over topographies is pivotal to understanding mixing, dispersion, and particle transport in environmental and engineering flows. A variety of natural terrains exhibit low-order complexity shaped by several factors, including wind-driven erosion and rain. Some low-order topographies also show low-order roughness; desert dunes with ripples are illustrative examples. In those cases, the specific role of ripples in the dynamics of near-wall and boundary-layer turbulence and particulate transport remains unclear. Sinusoidal walls have been used as simple configurations to uncover dominant flow features over topographies.

Studies of smooth sinusoidal walls have examined a broad range of phenomena, including recirculation and separation in the lee of crests (e.g., [1,2]), the influence of wave amplitude-to-wavelength ratio on the separated shear layer [3,4], turbulence structure in the inner and outer regions (e.g., [5–7]), momentum transport [8], and large-scale coherent motions identified via proper orthogonal decomposition [9,10]. These studies demonstrate that the adverse pressure

*Contact author: lpchamo@illinois.edu

gradient (APG) developing over the uphill section of the wave strongly modulates the turbulence dynamics. In particular, the flow decelerates toward the crest and becomes susceptible to separation downstream, leading to the formation of a shear layer characterized by elevated Reynolds stresses and enhanced turbulence production. A comprehensive review of turbulent flow over topography is given by Belcher and Hunt [11].

Surface roughness also modifies the mean momentum balance, near-wall turbulence structure, and coherent motions. Direct numerical simulations (DNS) of channels with transverse square bars show that element-scale separation and sheltering govern the balance between form drag and skin friction and alter Reynolds stresses throughout much of the boundary layer [12–15]. Sinusoidal roughness imposed on channel walls produces a shear layer whose characteristic velocity scale collapses drag and turbulence statistics across amplitude and wavelength [16]. Comparisons of two-dimensional (2D) and three-dimensional (3D) roughness reveal that 2D elements generate larger-scale motions and a stronger outer-layer response than their 3D counterparts [17,18], because the spanwise continuity of 2D elements promotes organized hairpinlike packet structures above the roughness [18,19]. These previous efforts show that roughness reorganizes near-wall turbulence through element-scale separation and modified coherent motions, often altering momentum transfer well beyond the immediate vicinity of the surface. Such insights are directly relevant to the present work, which examines the interaction between small-scale roughness and large-scale topography.

Despite these advances on both fronts, the combined effect of surface roughness superimposed on wavy topography has received comparatively little attention. Experimental work by Djenidi *et al.* [20] showed that 2D transverse-bar roughness amplifies Reynolds shear stress in the outer layer and reorganizes turbulent structures relative to a smooth wall, findings corroborated by DNS studies [13–15]. However, these studies considered flat-wall configurations with a nominally zero pressure gradient. On a wavy wall, the flow alternates between favorable pressure gradient (FPG) and APG regions within each wavelength. The APG region, where the separated shear layer forms and turbulence production peaks, is especially sensitive to modifications in the near-wall velocity field. It therefore remains unclear how even modest, low-order roughness alters the balance between ejection and sweep events, Reynolds shear stress, and turbulent kinetic energy (TKE) production within this APG segment. Understanding these interactions is not only of fundamental interest but also has practical implications for sediment transport, atmospheric boundary layers over complex terrain, and biofouled engineering surfaces.

The wavy-wall geometry employed here follows Hamed *et al.* [21], who characterized the fully turbulent boundary layer over 2D and 3D sinusoidal walls of the same amplitude-to-wavelength ratio and documented the separated shear layer, Reynolds stress distributions, and integral length scales in the developed flow. Their smooth-wavy-wall results [21,22] therefore provide a direct baseline for the present study, enabling the effects of the superimposed roughness to be isolated from the underlying topography-induced dynamics.

Here, we experimentally investigate the impact of 2D sinusoidal roughness on 2D sinusoidal topographies. We use very-high-resolution particle image velocimetry (PIV) in a refractive-index-matching (RIM) flume to characterize the flow dynamics within a wall-normal plane. The experimental setup is described in Sec. II, analysis and discussion are given in Sec. III, and main remarks are given in Sec. IV.

II. EXPERIMENTAL SETUP

The experiments were conducted in a 2.5-m-long, 112.5 mm × 112.5mm cross-section closed-loop, RIM flume. The fluid consisted of a NaI aqueous solution ∼63% by weight, density $\rho = 1800$ kg m^{-3}, and a kinematic viscosity $\nu = 1.1 \times 10^{-6}$ m^2 s^{-1}. The solution's refractive index was fine-tuned to match that of the wall using temperature control; this made the walls nearly invisible and allowed flow measurements in the troughs and very near the wall. For additional information about this technique, see Blois *et al.* [23] and Bai and Katz [24].

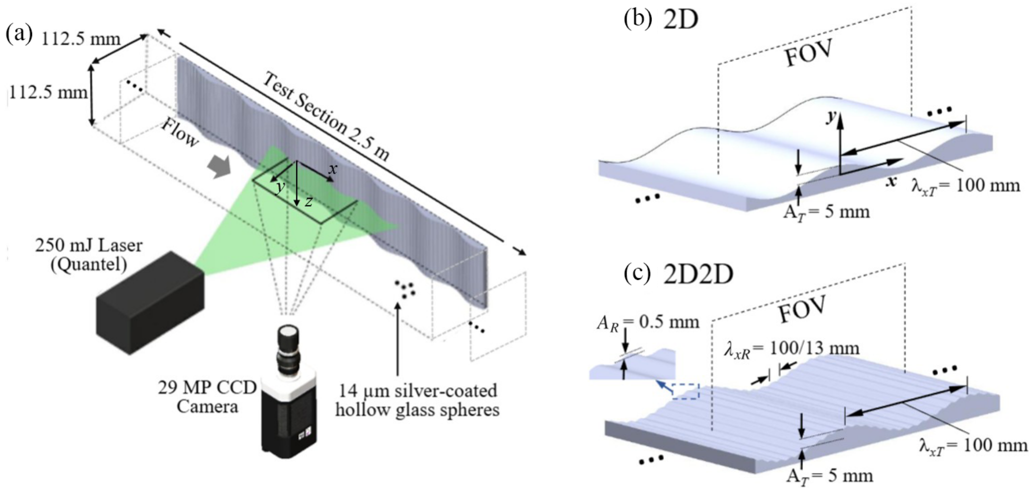

FIG. 1. (a) Basic schematic of the experimental setup illustrating placement of wavy walls in channel and PIV systems. (b), (c) Dimensions of the sinusoidal walls with low-order topographies and low-order roughness: (b) Smooth 2D topography (2D case) and (c) 2D topography with 2D roughness (2D2D case).

Two kinds of topographies studied here are cast from urethane resins using hydrodynamically smooth molds. The topographies were attached to the back wall of the RIM channel, spanning its full length and preceded by a 100-mm flat plate, which had an elliptical leading edge, and the elevation of the flat plate is set to the average wave height to minimize flow disturbances. Schematics of the experimental setups are shown in Fig. 1(a), and indicate the coordinate system. The base single-mode wavy-wall topography has a geometry $\sigma(x)$ consisting of large-scale sinusoidal waves, following the coordinate system defined in Fig. 1(b), given by

$$\sigma_{2D}(x) = A_T \cos(2\pi x/\lambda_{xT}), \tag{1}$$

where $A_T = 5$ mm is the amplitude of the large-scale topography, and $\lambda_{xT} = 100$ mm is the wavelength of the large-scale topography, which leads to amplitude-to-wavelength ratios of $A_T/\lambda_{xT} = 0.05$. The base topographies were set to match those used in Hamed *et al.* [21,22].

An additional small-scale 2D sinusoidal roughness with amplitude A_R and wavelength λ_{xR} of $A_R/A_T = 1/10$ and $\lambda_{xR}/\lambda_{xT} = 1/13$ was superimposed over the large-scale base case, creating a two-mode topography with the low-order small-scale roughness imposed on the large-scale wavy-wall base (henceforth 2D2D) is described by

$$\sigma_{2D2D}(x) = A_T \cos(2\pi x/\lambda_{xT}) + A_R \cos(2\pi x/\lambda_{xR}). \tag{2}$$

The two topographies, $\sigma_{2D}(x)$ and $\sigma_{2D2D}(x)$, are illustrated in Figs. 1(b) and 1(c). Flow statistics were studied at a bulk Reynolds number based on the bulk velocity, U_b, and channel half-heights $H/2$ were $\mathrm{Re} = U_b H/2\nu = 38\,400$ ($\approx 4 \times 10^4$). Additional complementary low Re results with an order smaller Reynolds number at $\mathrm{Re} = 3840$ ($\approx 4 \times 10^3$) are given in Sec. III E. Here U_b is defined following Hudson *et al.* [6] as shown in Eq. (3):

$$U_b = \frac{\int_0^{\lambda_x} \int_\sigma^{H/2} U \, dy \, dx}{\int_0^{\lambda_x} \int_\sigma^{H/2} dy \, dx}, \tag{3}$$

where $U = \langle u \rangle$ is the time-averaged streamwise velocity and the conditions are set to be identical to related studies of Hamed *et al.* [21,22]. With $k = A_T$ taken as the effective roughness height, one can estimate the equivalent sand-grain-based roughness k_s for sinusoidal roughness by $k_s \approx 7.3k\ \mathrm{ES}^{0.45}$ [25], where ES is the effective slope and ES = 0.2 and 0.26 [16], resulting is an estimated

$k_s \approx 0.017$ and 0.019 m for the 2D case and 2D2D case, respectively. The Reynolds number based on k_s for the 2D base case is $k_s^+ = k_s u_\tau/\nu \approx 493$ and $k_s^+ \approx 78$ for the high and low Reynolds number cases, respectively, with both exceeding the fully rough threshold of $k_s^+ > 70$. Here u_τ is estimated following Hamed *et al.* [21] by extrapolating $\langle -u'v' \rangle$ from the outer layer using profiles obtained over the entire large-scale topography wavelength (i.e., $x/\lambda_x \in [0, 1]$) and collapsing them such that $-\langle u'v' \rangle / u_\tau^2 = 1$ toward $y = 0$.

Flow-field characterization is achieved by performing PIV at the x-y plane. Additional PIV measurements in the x-z plane were conducted to verify negligible sidewall effects, yielding a sidewall boundary-layer thickness of $\delta_{\text{side}}/H \approx 0.08$ at the measurement location. The field of view (FOV) starts at $\sim 15\lambda_{xT}$ from the inlet, allowing the flow to approach developed condition with minimum streamwise variation [21]. The flow was seeded with 14 -µm silver-coated hollow glass sphere tracer particles, with a density of 1700 kg m^{-3}, and characterized with a high-resolution PIV within an x-y plane in the developed region extending over a wavelength. The 160 mm × 107 mm FOV was illuminated with a 1-mm-thick laser sheet using a 250-mJ pulse^{-1} double-pulsed laser from Quantel.

Four thousand image pairs were collected for each scenario at a frequency of 1 Hz with a 29-MP, 12-bit, frame-straddle, CCD camera. A recursive cross-correlation method was applied to interrogate the image pairs via insight 4G software from TSI. The final interrogation window had a size of 24 pixels × 24 pixels with 50% overlap, resulting in a vector grid spacing of $\Delta x = \Delta y \approx 200$ µm.

III. RESULTS

In this section we examine how the superposition of small-scale, low-order two-dimensional sinusoidal roughness on a large-scale wavy wall modifies the flow. Wall-normal planes within the fully developed region are analyzed using turbulence statistics, energy budgets, and quadrant decomposition to quantify the modulation induced by the small-scale roughness and to characterize the flow over the combined topographies in detail.

A. Turbulence statistics

The influence of the small-scale sinusoidal roughness on the corresponding large-scale sinusoidal topography is first assessed via the mean velocities $U = \langle u \rangle$ and $V = \langle v \rangle$, where $\langle \cdot \rangle$ is the time-average operator. Despite the distinct topographical surface variation, the mean streamwise velocity varies little between configurations (Fig. 2). By contrast, the wall-normal component exhibits clear differences between the favorable and adverse pressure-gradient regions (FPG and APG). On the FPG side of the 2D2D case, locally enhanced V occurs immediately adjacent to the small-scale roughness; on the APG side of the 2D2D case, attenuation of V at $y/\delta \approx 0.2$ is observed compared to the 2D case, where δ denotes the boundary-layer thickness at the beginning of the field of view, defined from the mean streamwise velocity profiles by $u(\delta) = 0.99U_b$; a value of $\delta/A_T \approx 9.6$ is obtained for both configurations. This suggests a weaker detached shear layer in the 2D2D configuration compared with the 2D case.

The Contours of the two-dimensional approximation of turbulent kinetic energy (TKE$_{2D}$), where $k_{2D} = \frac{1}{2}\langle u'u' + v'v' \rangle$ and Reynolds shear stress (RSS) $-\langle u'v' \rangle$ (Fig. 3) corroborate this inference, showing a weaker separated shear layer on the APG side when small-scale roughness is present, where $u' = u - U$ and $v' = v - V$ are the velocity fluctuations. The roughness-induced changes are concentrated in the APG segment $x/\lambda_x \in [0.1, 0.5]$, where the shear stress is reduced; effects are minor under FPG and near the crest of the large-scale topography. Profiles of the normal stresses $\langle u'u' \rangle$ and $\langle v'v' \rangle$ (Fig. 4) further highlight these trends. In general, the 2D case exhibits larger peak values, with the greatest discrepancy at $x/\lambda_x \simeq 0.3$, coincident with the onset of large-scale shear-layer development. The enhancement of $\langle v'v' \rangle$ in the 2D case persists over the entire wavelength, largely independent of the local pressure gradient, whereas differences in $\langle u'u' \rangle$ are mainly confined to the APG region (i.e., $x/\lambda_x \in [0, 0.5]$).

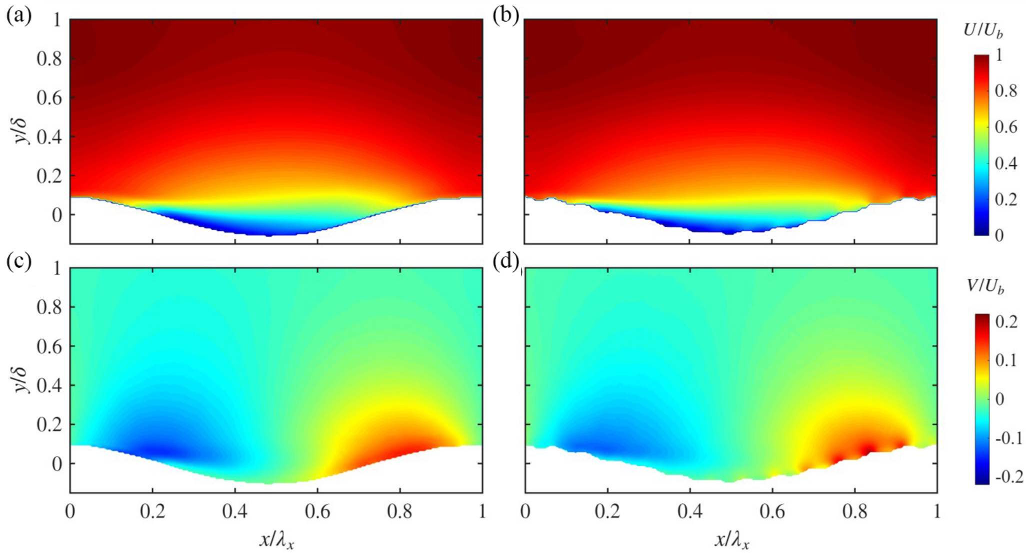

FIG. 2. Nondimensional time-averaged velocity fields over (a), (c) 2D and (b), (d) 2D2D topographies: (a), (b) mean streamwise velocity U/U_b and (c), (d) mean wall-normal velocity V/U_b.

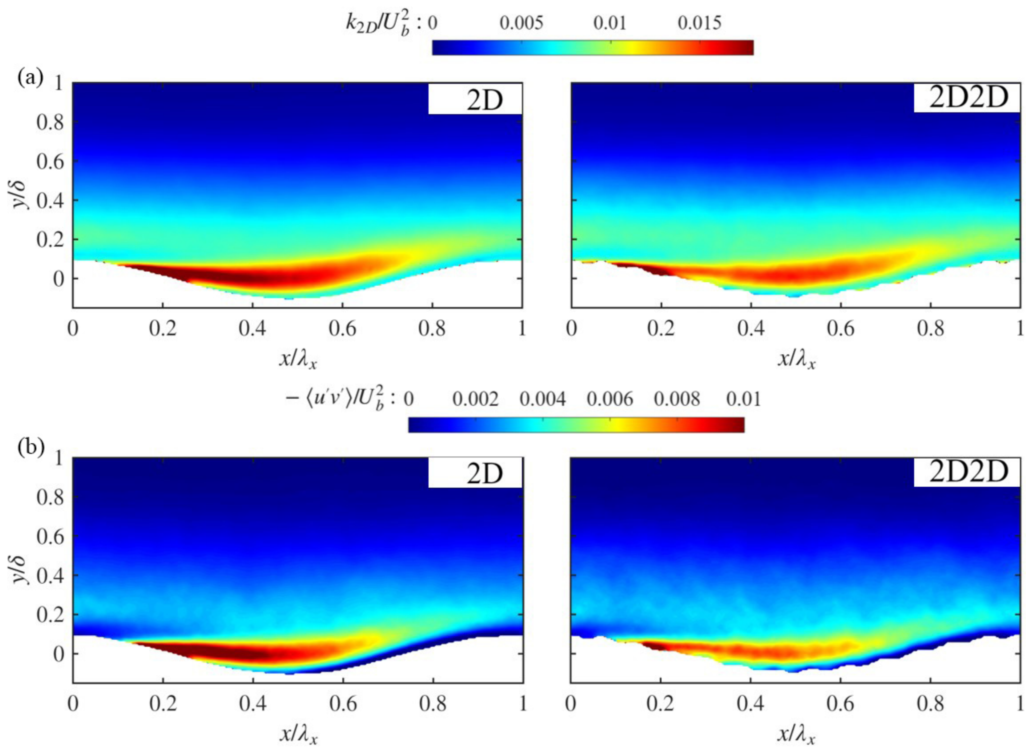

FIG. 3. Normalized contour of (a) TKE_{2D} and (b) RSS over 2D and 2D2D topographies.

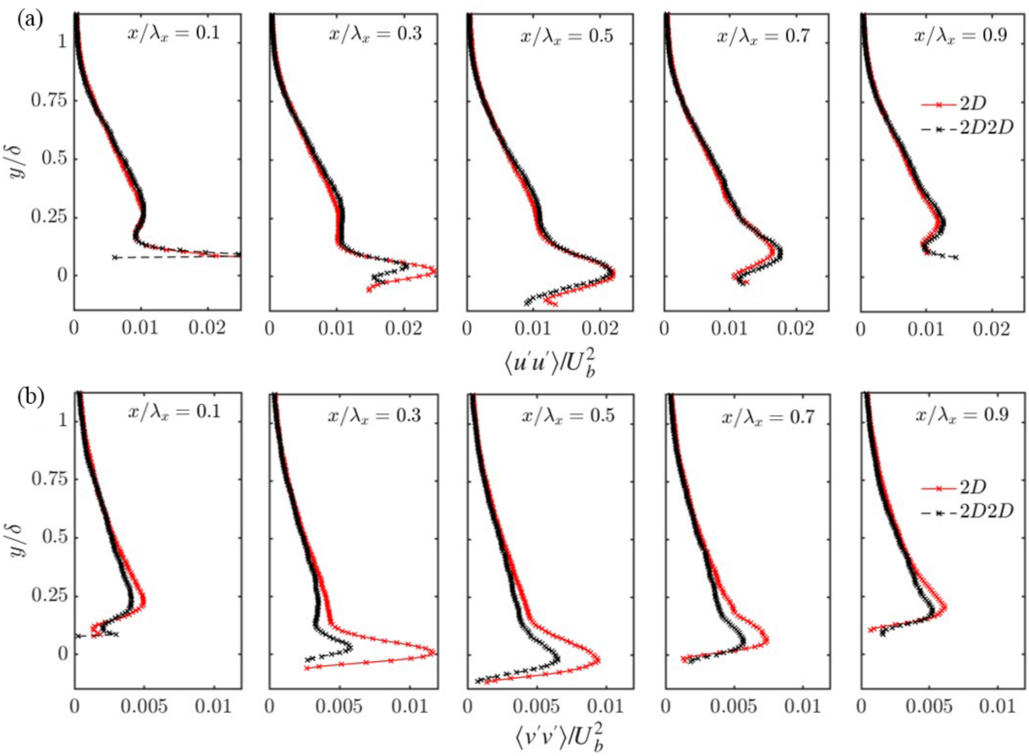

FIG. 4. Nondimensional vertical profiles of (a) $\langle u'u' \rangle / U_b^2$ and (b) $\langle v'v' \rangle / U_b^2$ over the 2D and 2D2D topographies along the large-scale topography wavelength.

To uncover near-wall energy redistribution by the small-scale topography, Fig. 5 presents representative instantaneous fields showing the contours of u'/U_b superposed on the in-plane velocity vectors. The 2D2D configuration demonstrates more prominent, larger-scale coherent patterns immediately above the surface than the 2D case, particularly for $y'/\delta \simeq 0.2$ (see the red dashed regions in Fig. 5). Here $y'(x) = y - \sigma(x)$ denotes the local wall-normal distance from the surface. These near-wall structures likely interact with large-scale shear-layer formation and may be the cause of the reduced TKE_{2D} and RSS observed for 2D2D in Fig. 3.

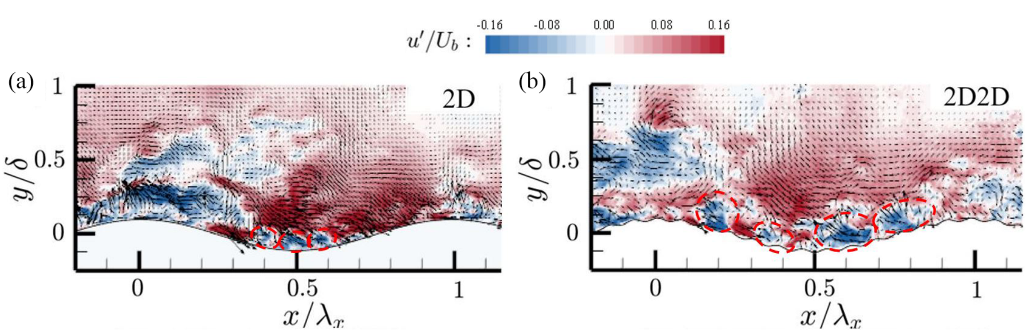

FIG. 5. Instantaneous fields of velocity fluctuations $u'\hat{i} + v'\hat{j}$ superimposed on contours of u'/U_b for the (a) 2D and (b) 2D2D topographies. For clarity, the figures only show every four vectors.

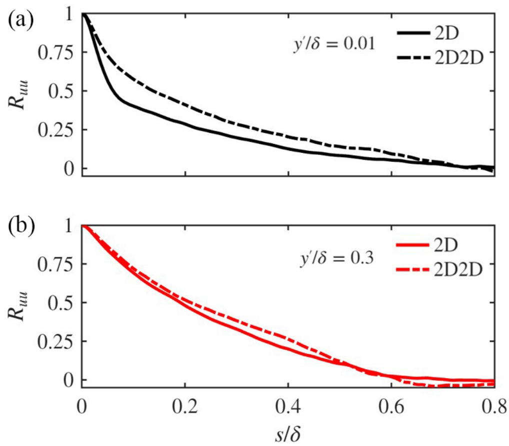

FIG. 6. (a), (b) Two-point vertical correlation function of the streamwise velocity fluctuations, $R_{uu}(s)$ taken at $x/\lambda_x = 0.3$ at a distance from the surface of (a) $y'/\delta = 0.05$ and (b) $y'/\delta = 0.3$. (c) Integral length scale L_u/δ streamwise distribution at two distances from the surface.

B. On the coherent structures

Two-point spatial correlations of the streamwise velocity, R_{uu}, are computed to estimate the length scales of the near-wall coherent motions and to quantify the features visible in Fig. 5. The one-dimensional autocorrelation evaluated along a wall-normal line originating at y_0 is defined as [26]

$$R_{uu}(s) = \frac{\langle u'(y_0, t), u'(y_0 + s, t)\rangle}{\langle u'(y_0, t)^2\rangle}, \tag{4}$$

where s is the wall-normal separation. Representative wall-normal correlations at two distances from the surface, $y'/\delta = 0.01$ and 0.3, within the APG region at $x/\lambda_x = 0.3$, are shown in Figs. 6(a) and 6(b) for the 2D and 2D2D walls. The wavy roughness exerts a clear influence on the near-wall organization, showing a systematically larger R_{uu} for the 2D2D case than for the 2D case (the same trend holds at other x/λ_x, not shown for brevity).

To quantify these differences we consider the integral length scale,

$$L_u = \int_0^\infty R_{uu}(s)ds, \tag{5}$$

evaluated in practice up to the separation with a sufficiently low $R_{uu} = 0.05$ [27]. The resulting L_u/δ across one wavelength of the topography is shown in Fig. 6(c).

Very near the wall (i.e., $y'/\delta = 0.01$), L_u is consistently larger over the 2D2D topography for all $x/\lambda_x \in [0, 1]$. This indicates that larger scale coherent motions were induced by the low-order roughness very close to the surface as the higher wave number roughness induces larger hairpinlike packets compared to the smooth 2D topography, consistent with the instantaneous velocity fields in Fig. 5 and with observations in zero pressure gradient boundary layers [18]. Moreover, Fig. 6 also reveals a larger near-wall coherent structure in the FPG region than in the APG portions at $y'/\delta = 0.01$.

By contrast, farther from the wall (i.e., $y'/\delta = 0.3$), the integral scale is governed primarily by the developing shear layer. In this region, the variation of L_u with x/λ_x is weak and the difference between the 2D and 2D2D cases is negligible, indicating a reduced sensitivity to the topography-induced pressure gradient modulation. To elucidate how the larger near-wall coherent structures in the 2D2D configuration weaken the overall TKE and the RSS shown in Fig. 3, the TKE budget and quadrant analysis are examined next.

C. Turbulent kinetic energy budget

The turbulent kinetic energy budget is explored to uncover the particular impact of the low-order roughness. The transport equation of two-dimensional approximation of turbulent kinetic energy reads

$$\frac{DE}{Dt} = P + T + \Pi + D - \varepsilon. \tag{6}$$

Here P is the in-plane k production, T is the turbulent transport, Π is the pressure transport, D is the viscous diffusion, and ε is the dissipation. Two-dimensional, in-plane approximations, assuming a steady, two-dimensional flow, and neglecting spanwise gradients in the mean quantities, follow Kruse *et al.* [10] and Hudson *et al.* [6]:

$$P = -\langle u'v'\rangle\frac{\partial U}{\partial y} - \langle u'u'\rangle\frac{\partial U}{\partial x} - \langle u'v'\rangle\frac{\partial V}{\partial x} - \langle v'v'\rangle\frac{\partial V}{\partial y}, \tag{7}$$

$$T \approx -\frac{1}{2}\frac{\partial\langle u'u'v'\rangle}{\partial y} - \frac{1}{2}\frac{\partial\langle v'v'v'\rangle}{\partial y}, \tag{8}$$

$$\varepsilon \approx 6\nu\left(\left\langle\left(\frac{\partial u'}{\partial x}\right)^2\right\rangle + \left\langle\left(\frac{\partial u'}{\partial y}\right)^2\right\rangle + \left\langle\left(\frac{\partial u'}{\partial y}\frac{\partial v'}{\partial x}\right)\right\rangle\right). \tag{9}$$

The dissipation is first estimated under the usual assumption that the smallest-scale motions are statistically stationary and locally isotropic and are weakly coupled to the large scales; we denote this estimate by $\varepsilon_{\mathrm{ISO}}$ [28,29]. A basic check of local isotropy is provided by $\langle(\partial u'/\partial x)^2\rangle \approx \langle(\partial v'/\partial y)^2\rangle$. Despite the high PIV resolution, dissipation remains under-resolved, as Kolmogorov scale is estimated to be $\eta = (\nu^3/\varepsilon)^{1/4} \approx 60$ µm, whereas the PIV grid spacing is approximately 3η. An large eddy simulations (LES)-based surrogate follows Sheng *et al.* [30] and Cheng *et al.* [31], which treats the PIV resolution as the filter scale and estimates the subgrid dissipation via a Smagorinsky closure under dynamic equilibrium as a complement. This alternative yields consistent trends with the $\varepsilon_{\mathrm{ISO}}$. All budget terms are examined except Π and D as the pressure term is inaccessible, and viscous diffusion is expected to be appreciable only within the viscous sublayer [32].

Figure 7 presents contours of the total production P and of the first two terms in Eq. (7). The total P [Fig. 7(a)] shows clear signatures of the sinusoidal roughness in the near-wall flow, with systematically weaker production on the APG side. In addition, a localized region of enhanced P appears immediately above the superposed small-scale roughness [highlighted by the small dashed circles in Fig. 7(a)], indicating that the roughness triggers coherent motions at its comparable scales. The low-order roughness also induced a streamwise velocity gradient, leading to a non-negligible streamwise acceleration term $-\langle u'v'\rangle\partial U/\partial x$ [Fig. 7(c)] near the wall, showing positive P in the near-wall region consistent with a shear layer generated by the small-scale roughness demonstrated in Djenidi *et al.* [20].

Streamwise variation of vertically averaged budget terms averaging over the topography sublayer, $y/\delta \lesssim 0.45$, is shown in Fig. 8 and denoted by $\langle\cdot\rangle_{\Delta y}$. The bulk $\langle P\rangle_{\Delta y}$ peaks slightly downstream from the large-scale crest at $x/\lambda_x \approx 0.2$, consistent with a crest-generated shear layer that supports turbulence over 2D wavy walls [6,33]. In the 2D2D configuration, this peak shifts closer to the crest and $\langle P\rangle_{\Delta y}$ is reduced in the APG region relative to the 2D case, suggesting that the larger near-wall coherent structures induced by the small-scale roughness may weaken the development of the large-scale shear layer. The streamwise variation of $\langle T\rangle_{\Delta y}$ appears significant only within $0.1 \lesssim x/\lambda_x \lesssim 0.3$ [Fig. 8(b)], where a positive peak is followed by a negative one in both cases. The magnitude and location of these peaks mirror those of $\langle P\rangle_{\Delta y}$, with the 2D case exhibiting a larger transport peak to diffuse higher P. The negative peaks indicate energy depletion downstream from the production maximum, in line with the behavior reported by Hong *et al.* [32].

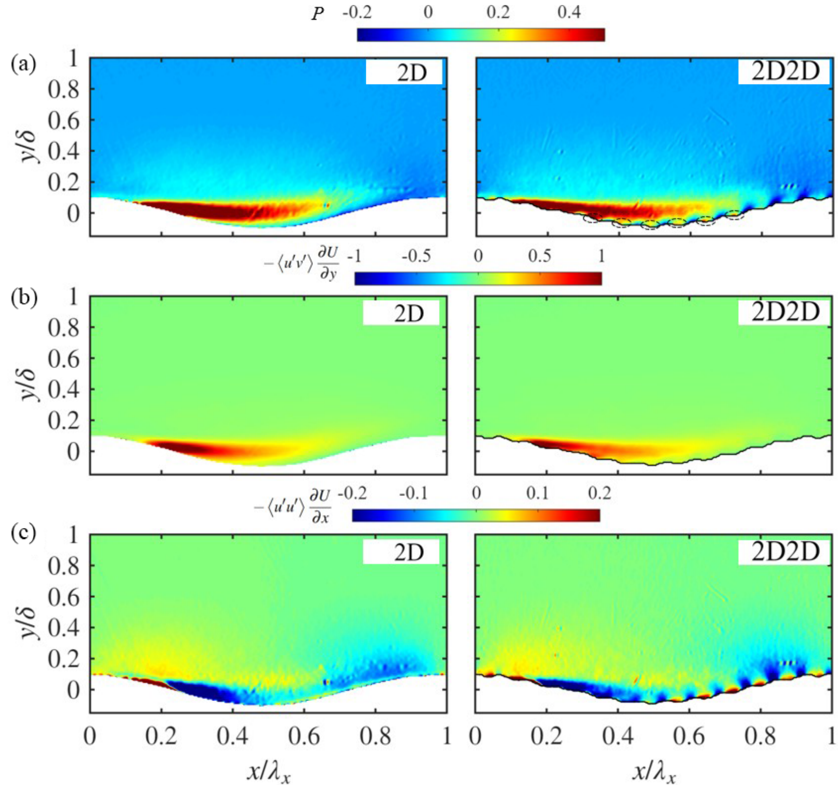

FIG. 7. (a) In-plane turbulence kinetic energy production, P, with contributions from (b) $-\langle u'v'\rangle \frac{\partial U}{\partial y}$ and (c) $-\langle u'u'\rangle \frac{\partial U}{\partial x}$ for the (left) 2D and (right) 2D2D topographies.

Finally, Fig. 8(c) compares two dissipation estimates, $\varepsilon_{\mathrm{ISO}}$ and an axisymmetry-based surrogate about the streamwise direction, $\varepsilon_{\mathrm{ASX}}$ [34], given by

$$\varepsilon_{\mathrm{ASX}} \approx \nu\left(-\left\langle\left(\frac{\partial u'}{\partial x}\right)^2\right\rangle + 8\left\langle\left(\frac{\partial v'}{\partial y}\right)^2\right\rangle + 2\left\langle\left(\frac{\partial u'}{\partial y}\right)^2\right\rangle + 2\left\langle\left(\frac{\partial v'}{\partial x}\right)^2\right\rangle\right). \tag{10}$$

The two estimates agree closely, with only minor deviations near the topography valley (the axisymmetry surrogate being slightly lower). In both 2D and 2D2D cases the dissipation weakens

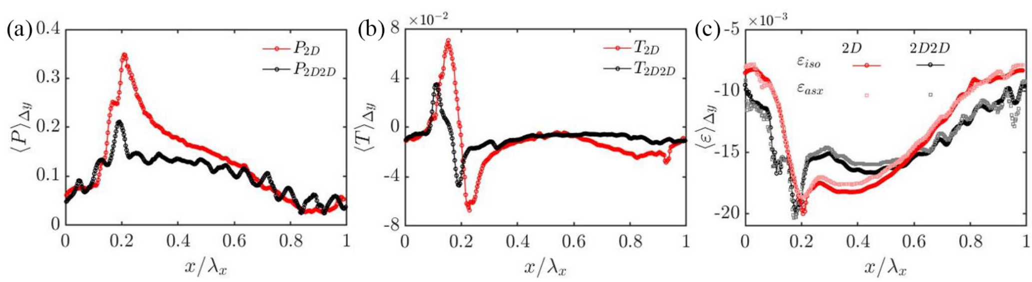

FIG. 8. E budget terms averaged over the wall-normal direction within topography sublayer for the 2D and 2D2D topographies along the wavelength. (a) Production, $\langle P\rangle_{\Delta y}$, (b) transport, $\langle T\rangle_{\Delta y}$, and (c) dissipation, $\langle \varepsilon\rangle_{\Delta y}$.

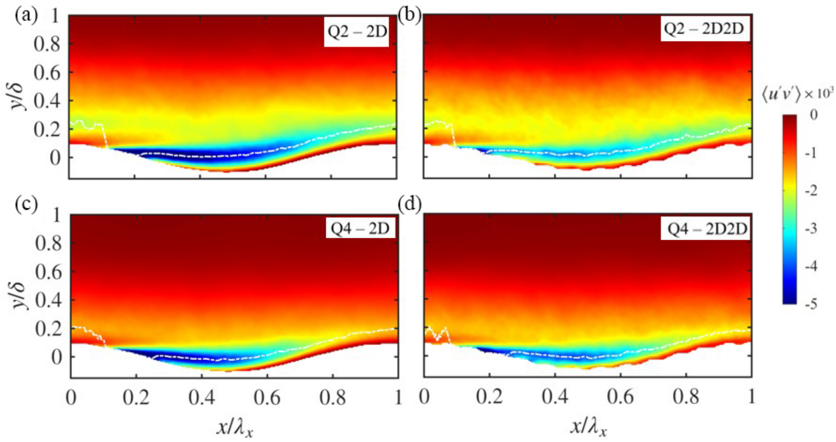

FIG. 9. Quadrant decomposition of the kinematic shear stress $\langle u'v'\rangle$. Ejections ($Q2$) for the (a) 2D and (b) 2D2D cases; sweeps ($Q4$) for the (c) 2D and (d) 2D2D topographies.

over the crest and peaks near $x/\lambda_x \approx 0.2$, close to the production maximum. Notably, the superposed small-scale roughness in 2D2D redistributes dissipation, yielding higher levels (in magnitude) near the crest and lower levels within the APG section compared with the 2D counterpart.

D. Quadrant decomposition

A quadrant-hole analysis is carried out to further access how the superimposed low-order roughness generates and redistributes shear stress relative to the base large-scale 2D topography. Following the classical framework of Lu and Willmarth [35] as implemented by Nolan *et al.* [36], the velocity fluctuations are decomposed into four quadrants as outward interactions ($Q1$: $u' > 0$ and $v' > 0$), ejections ($Q2$: $u' < 0$ and $v' > 0$), inward interactions ($Q3$: $u' < 0$ and $v' < 0$), and sweeps ($Q4$: $u' > 0$ and $v' < 0$).

Figure 9 shows contours of the dominant sweep and ejection activity for the 2D and 2D2D scenarios, overlaid with the shear-layer centerline (white-dashed line) obtained by locating the local maxima of $-\langle u'v'\rangle$ [6]. Together with the quadrant decomposed shear-layer centerline profiles in Fig. 10, these results indicate that the small-scale roughness reduces the shear stress by weakening

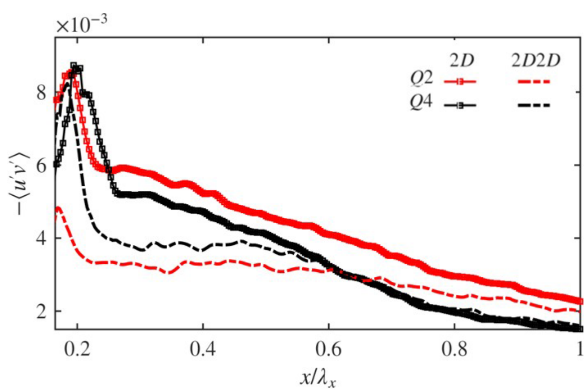

FIG. 10. Quadrant decomposed $-\langle u'v'\rangle$ profiles taken at the shear-layer centerline for the 2D and 2D2D cases.

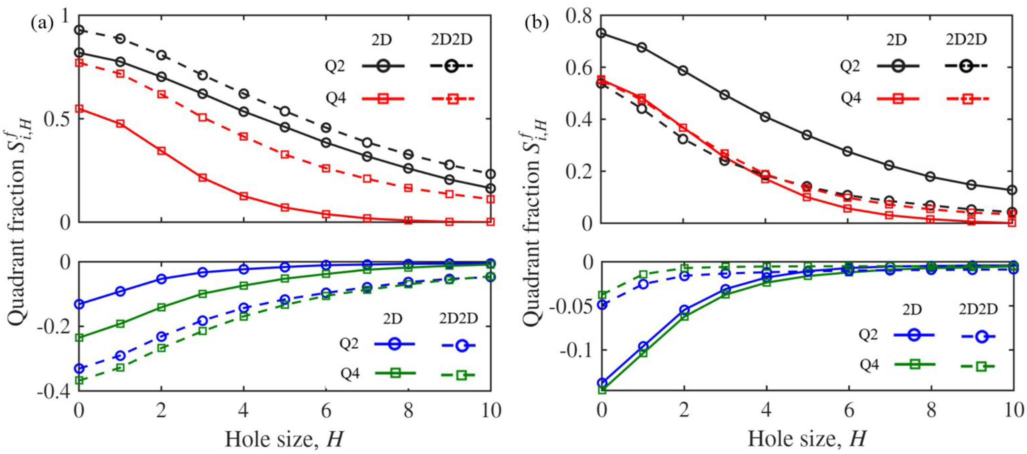

FIG. 11. Quadrant fraction within topography sublayer as a function of hole size H for (a) $x/\lambda_x \in [0, 0.2]$ and (b) $x/\lambda_x \in [0.2, 0.5]$.

the shear layer primarily via a suppression of $Q2$ ejections, showing a nearly 50% lower $Q2$ at the shear-layer origin and the $Q2$ remains ≈25% lower for $x/\lambda_x \in [0.3, 0.5]$.

To quantify event intensity across scales, a hyperbolic-hole method is employed. The so-called hyperbolic hole, H, splits regions with hyperbolic curves defined by $|u'v'| = H|\langle u'v'\rangle|$ [37]. The mean quadrant events as a function of hole size H can then be defined as follows:

$$S_{i,H} = \frac{1}{T_0}\int_0^{T_0} u'(x, y, t)v'(x, y, t)I_{i,H,t}(u', v')dt, \tag{11}$$

where $i \in 1, 2, 3, 4$ indicates events in a specific quadrant and T_0 is the sampling period, and a piecewise function $I_{i,H,t}$ is introduced for conditional sampling, where

$$I_{i,H,t}(u', v') = \begin{cases} 1 & \text{for } (u', w') \text{ in quadrant } i \text{ and } |u'v'| \geqslant H|\langle u'v'\rangle| \\ 0 & \text{otherwise} \end{cases} \tag{12}$$

We report the normalized quadrant fraction $S^f_{i,H} = S_{i,H}/S$, with $S = |\langle u'v'\rangle|$. The quadrant fraction $S^f_{i,H}$ before the large-scale shear-layer formation for $x/\lambda_x \in [0, 0.2]$ and over the developed shear layer $x/\lambda_x \in [0.2, 0.5]$ within the topography sublayer are shown in Fig. 11.

Outside of the developed shear-layer region, the 2D2D topography exhibits larger $Q2$ and $Q4$ fractions than the 2D counterpart as seen in Fig. 11(a), indicating that the added low-order roughness promotes sweeps and ejections near wall due to enhanced transport in the immediate vicinity of the element [13,38,39]. This tendency persists for all scales across hole sizes. In contrast, at the APG region with developed shear-layer region $x/\lambda_x \in [0.3, 0.5]$, the 2D2D case shows a reduced $Q2$ fraction with a similar $Q4$ level to the 2D case. The decrease in $Q2$ frequency and strength accounts for the lower Reynolds shear stress of 2D2D and, through the first TKE production term $-\langle u'v'\rangle\partial U/\partial y$, contributes to the reduced TKE production documented in Fig. 8, showing that larger near-wall coherent structures disturbed the development of the shear layer in the APG region [40].

To illustrate the impact of low-order roughness on the flow structures, we compute quadrant-conditioned two-point correlations at the reference location (x_0, y_0), defined as a generalized form of Eq. (4) as

$$R_{ij}(x_0, y_0) = \frac{\langle u'_i(x_0, y_0)u'_j(x_0 + \Delta x, y_0 + \Delta y)\rangle}{\sqrt{\langle u'_i(x_0, y_0)^2\rangle}\sqrt{\langle u'_j(x_0 + \Delta x, y_0 + \Delta y)^2\rangle}}. \tag{13}$$

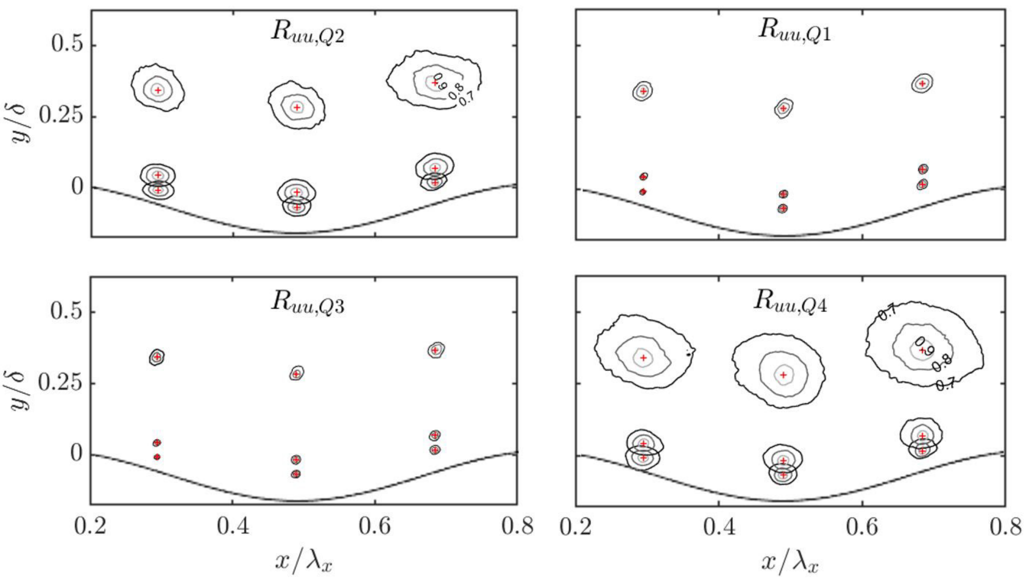

FIG. 12. Quadrant-conditioned streamwise velocity two-point correlation R_{uu} for the 2D topography at local heights $y' = 0.05$, 0.1, and 0.5 (+ symbol).

Representative maps of R_{uu}, Q_i for the 2D wall at $x/\lambda_x = 0.3, 0.5, 0.7$ and four elevations $y'/\delta = 0.05, 0.1, 0.4$ are shown in Fig. 12. They reveal $Q1$- and $Q3$-conditioned structures limited to the roughness scale, whereas $Q2$ and $Q4$ structures attain integral-scale dimensions, with $Q1$, $Q3$ events showing a $L_u \sim \mathcal{O}(10^{-2}\delta)$ near the wall, while $Q2$, $Q4$ events demonstrate a $L_u \sim \mathcal{O}(10^{-1}\delta)$. As expected, $Q4$ structures are larger than their $Q2$ counterparts because sweeps import larger motions into the boundary layer, while ejections typically convey smaller structures to higher elevations [41]. Despite their smaller size, the relatively high duration fraction of $Q2$ events makes them major contributors to turbulence statistics. Additionally, the smaller $Q2$ structures are more susceptible to the larger scale near-wall coherent motions generated by the superimposed roughness, which explains the features of ejection event reduction for the 2D2D case observed in Figs. 10 and 11.

$Q2$- and $Q4$-conditional averaged R_{uu} for the 2D2D case in Fig. 13(a) shows systematically larger structures at all elevations as indicated by the quadrant conditioned L_u in Fig. 13(b), consistent with the increased integral scales in Fig. 6. The integral length scales of $Q1$ and $Q3$ events show negligible differences between the 2D2D and 2D cases and are not shown for brevity, as they

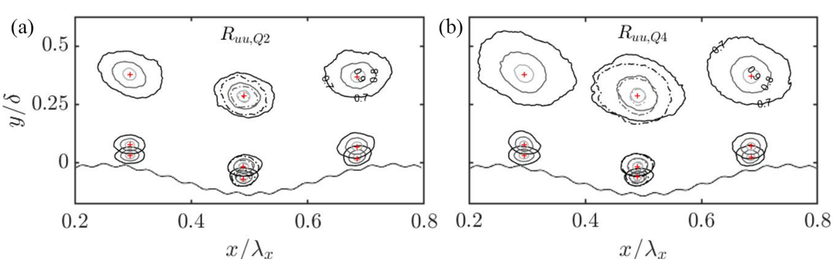

FIG. 13. (a) Quadrant conditioned streamwise velocity two-point correlation R_{uu} for the 2D2D case with respect to various reference points (marked by a + symbol); additional R_{uu} for the 2D case provided in dash-dotted lines at the large topography valley for comparison. (b) Quadrant-conditioned integral length scale computed for selected y' locations at $x/\lambda_x = 0.5$, (left) $Q2$-conditioned and (right) $Q4$-conditioned L_u.

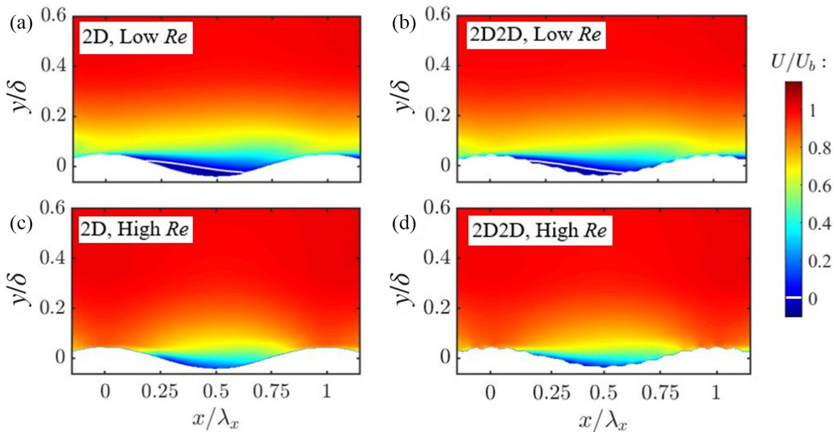

FIG. 14. Nondimensional time-averaged streamwise velocity fields U/U_b over the (a) 2D, low Re, (b) 2D2D, low Re, (c) 2D, high Re, and (d) 2D2D, high Re cases.

contribute minimally to the total RSS. The prevalence of larger near-wall structures in the 2D2D case leads to suppressed, weaker $Q2$ events. In terms of the TKE budget, this suppression diminishes the RSS magnitude $-\langle u'v'\rangle$ and thereby reduces the local production through the $-\langle u'v'\rangle\frac{dU}{dy}$ term. The quadrant-based weakening of $Q2$ activity is thus directly reflected in a lower P in the 2D2D configuration.

E. Complementary low Re Results

Complementary results at a lower Reynolds number are presented here. The low Re number case with Re $= 3840$ ($\approx 4 \times 10^3$) is approximately one decade smaller than the case discussed (Re $\approx 4 \times 10^4$).

The mean streamwise velocity contour in Fig. 14 highlights the Reynolds number effect. The low Re cases demonstrate a larger recirculation region downstream from the wavy-wall crest, showcasing a separation at $x/\lambda_x \approx 0.18$ and 0.16 and reattached at $x/\lambda_x \approx 0.63$ and 0.62 for the 2D and 2D2D cases, as indicated by the white $U = 0$ isoline superimposed on the contours. Despite the distinct base flow difference between the Reynolds numbers. The role of low-order roughness is similar and shows minimal impact on the streamwise bulk flow between the 2D and 2D2D cases.

A comparable conclusion holds for higher-order statistics. The RSS contour in Fig. 15 and the shear-layer centerline profile (Fig. 16) show that adding low-order roughness weakens the large-scale shear layer and shifts it slightly upstream relative to the 2D base case. This attenuation of shear-layer strength is markedly more pronounced at high Re, whereas only a modest reduction is observed at low Re.

The autocorrelation R_{uu} and integral length scale L_u in Fig. 17 indicate the formation of larger coherent structures very close to the surface in the 2D2D configuration. This behavior mirrors that at high Re, although the differences are more pronounced for high Re cases. Finally, the $Q2$ and $Q4$ quadrant contours in Fig. 18 and the associated quadrant-conditioned shear-layer centerline profiles in Fig. 19 show that the larger near-wall coherent structures in the 2D2D case suppress the large-scale shear layer by reducing the ejection events.

The results point to an essentially identical mechanism at both Reynolds numbers. The low-order roughness associated with the 2D2D topography promotes larger near-wall coherent motions, which, in turn, weaken the large-scale shear-layer development by diminishing $Q2$ ejections. This results in reduced turbulence production and smaller RSS in 2D2D compared with the smooth wavy

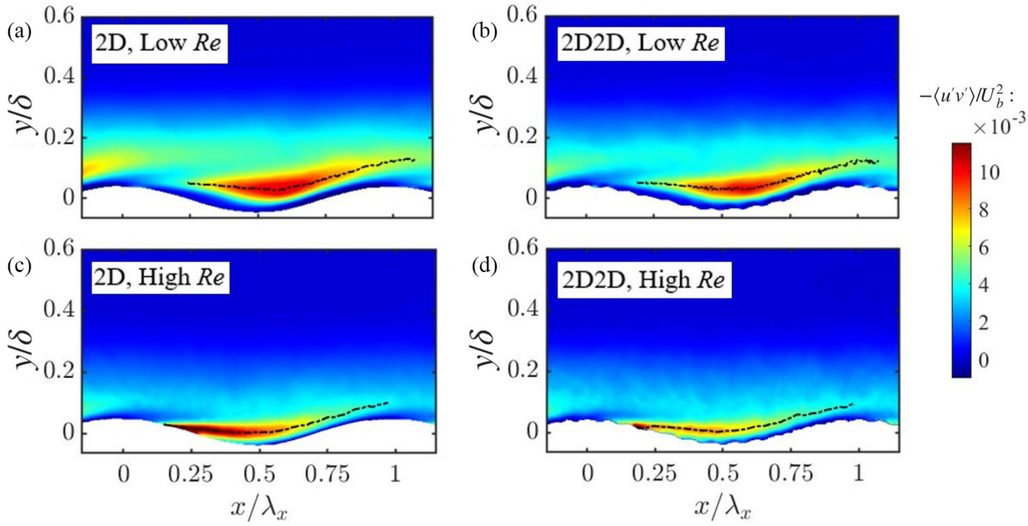

FIG. 15. Time-averaged kinematic shear stress $\langle u'v'\rangle/U_b$ for the (a) 2D, low Re, (b) 2D2D, low Re, (c) 2D, high Re, and (d) 2D2D, high Re cases. The dashed line indicates the centerline of the shear layer.

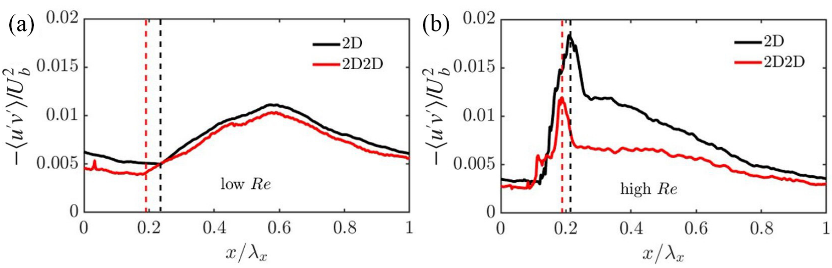

FIG. 16. Comparison between the 2D and 2D2D shear centerline kinematic shear stress profiles $-\langle u'v'\rangle/U_b$ for the (a) low Re and (b) high Re cases.

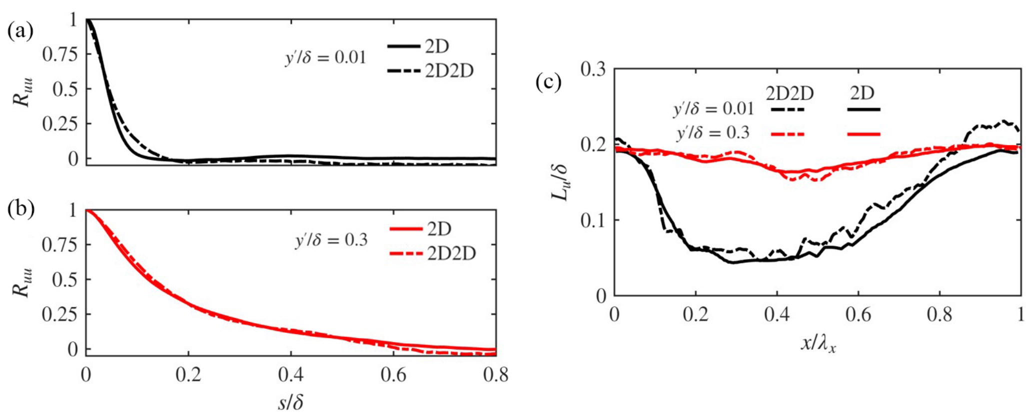

FIG. 17. (a), (b) Two-point vertical correlation function of the streamwise velocity fluctuations, $R_{uu}(s)$, taken at $x/\lambda_x = 0.3$ at a distance from the surface of (a) $y'/\delta = 0.05$ and (b) $y'/\delta = 0.3$. (c) Integral length scale L_u/δ streamwise distribution at two distances from the surface.

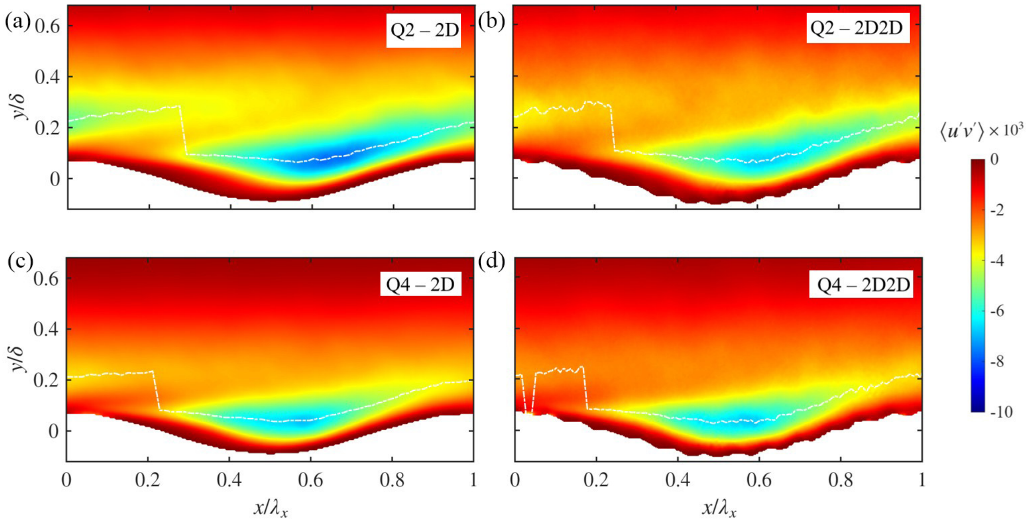

FIG. 18. Quadrant decomposition of the kinematic shear stress $\langle u'v' \rangle$. Ejections ($Q2$) for the (a) 2D and (b) 2D2D cases; sweeps ($Q4$) for the (c) 2D and (d) 2D2D topographies.

wall (2D case). The generation of near-wall coherence and the suppression of $Q2$ events are more prominent at high Re.

IV. REMARKS AND CONCLUSIONS

Laboratory experiments conducted in a refractive-index-matched facility, combined with high-spatial-resolution PIV, revealed the distinct modulation induced by low-order roughness on the flow over low-order sinusoidal topography. Analysis of second-order statistics, the TKE budget, and quadrant-conditioned quantities elucidated the mechanism by which a two-dimensional sinusoidal roughness superposed on a two-dimensional wavy wall (2D2D) modifies turbulence relative to its hydrodynamically smooth counterpart (2D). The inclusion of the smooth-topography baseline was essential for isolating near-wall contributions from the nonlocal modulation of the outer shear layer.

A central finding is that the imposed 2D sinusoidal roughness systematically reduces the Reynolds shear stress within the developed shear layer downstream from the topographic crest, compared with the smooth-wall case. Two-point streamwise velocity correlations, R_{uu}, and integral length scales, L_u, indicate the emergence of larger near-wall coherent motions triggered by the added roughness. These enhanced structures predominantly affect the adverse-pressure-gradient region, where the quadrant-hole analysis shows a marked suppression of ejection events. The reduced ejection activity weakens local TKE production and redistribution, leading to the observed attenuation of the separated shear layer for the 2D2D configuration.

At a lower Reynolds number, Re $\approx 4 \times 10^3$, a qualitatively similar behavior is observed, though the contrast between the 2D and 2D2D topographies diminishes, suggesting that the modulation strength scales with Reynolds number.

Overall, the results demonstrate that even modest, low-order roughness can reorganize turbulence over simple wavy surfaces through a sequential mechanism: the roughness geometry promotes the formation of larger coherent structures through the separation and reattachment cycle downstream from each roughness element [42]. These structures are associated with sweeplike events, in which high-momentum fluid is driven downward into the cavity region, in contrast to the ejection-dominated behavior typical of smooth walls.

The resulting sweep-dominated near-wall dynamics suppress and disrupt the original shear-layer separation [43,44] on the adverse pressure gradient side of the large-scale wavy topography, leading

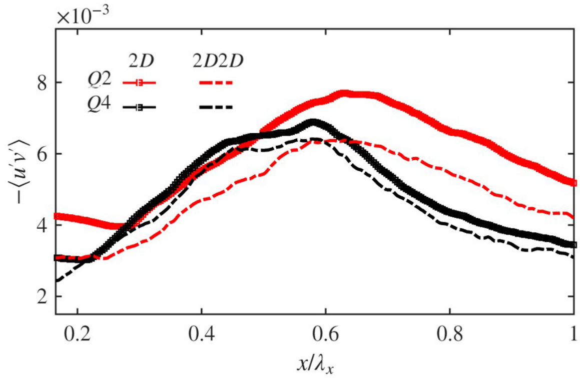

FIG. 19. Quadrant decomposed $-\langle u'v' \rangle$ profiles taken at the shear-layer centerline for the 2D and 2D2D cases.

to reduced turbulent kinetic energy and Reynolds shear stress. Quantifying these interactions provides a foundation for improved modeling of momentum and scalar transport over natural bedforms and engineered rough surfaces. Future work will address the influence of geometric singularities and temporally evolving topographies (e.g., migrating or oscillating surfaces) and will explore broader ranges of Re, amplitude, and wavelength ratios to develop predictive parametrizations of multiscale surface modulation effects.

ACKNOWLEDGMENTS

The experiments were performed in a facility built under the National Science Foundation Grant, Award No. CBET-0923106.

The authors report no conflict of interest.

DATA AVAILABILITY

The data supporting the findings of this article are available from the corresponding author upon reasonable request.

[1] D. P. Zilker and T. J. Hanratty, Influence of the amplitude of a solid wavy wall on a turbulent flow. Part 2. Separated flows, J. Fluid Mech. **90**, 257 (1979).

[2] J. Buckles, T. J. Hanratty, and R. J. Adrian, Turbulent flow over large-amplitude wavy surfaces, J. Fluid Mech. **140**, 27 (1984).

[3] J. D. Kuzan, T. J. Hanratty, and R. J. Adrian, Turbulent flows with incipient separation over solid waves, Exp. Fluids **7**, 88 (1989).

[4] H. S. Yoon, O. A. El-Samni, A. T. Huynh, H. H. Chun, H. J. Kim, A. H. Pham, and I. R. Park, Effect of wave amplitude on turbulent flow in a wavy channel by direct numerical simulation, Ocean Eng. **36**, 697 (2009).

[5] S. Nakagawa and T. J. Hanratty, Particle image velocimetry measurements of flow over a wavy wall, Phys. Fluids **13**, 3504 (2001).

[6] J. D. Hudson, L. Dykhno, and T. J. Hanratty, Turbulence production in flow over a wavy wall, Exp. Fluids **20**, 257 (1996).

[7] K. Bhaganagar, J. Kim, and G. Coleman, Effect of roughness on wall-bounded turbulence, Flow, Turbul. Combust. **72**, 463 (2004).

[8] S. Kuhn, C. Wagner, and P. R. von Rohr, Influence of wavy surfaces on coherent structures in a turbulent flow, Exp. Fluids **43**, 251 (2007).

[9] A. Günther and P. R. Von Rohr, Large-scale structures in a developed flow over a wavy wall, J. Fluid Mech. **478**, 257 (2003).

[10] N. Kruse, S. Kuhn, and P. R. von Rohr, Wavy wall effects on turbulence production and large-scale modes, J. Turbul. **7**, N31 (2006).

[11] S. E. Belcher and J. C. R. Hunt, Turbulent flow over hills and waves, Annu. Rev. Fluid Mech. **30**, 507 (1998).

[12] S. Leonardi, P. Orlandi, R. J. Smalley, L. Djenidi, and R. A. Antonia, Direct numerical simulations of turbulent channel flow with transverse square bars on one wall, J. Fluid Mech. **491**, 229 (2003).

[13] S.-H. Lee and H. J. Sung, Direct numerical simulation of the turbulent boundary layer over a rod-roughened wall, J. Fluid Mech. **584**, 125 (2007).

[14] T. Ikeda and P. A. Durbin, Direct simulations of a rough-wall channel flow, J. Fluid Mech. **571**, 235 (2007).

[15] J. H. Lee, H. J. Sung, and P.-Å. Krogstad, Direct numerical simulation of the turbulent boundary layer over a cube-roughened wall, J. Fluid Mech. **669**, 397 (2011).

[16] S. Ganju, S. C. C. Bailey, and C. Brehm, Amplitude and wavelength scaling of sinusoidal roughness effects in turbulent channel flow at fixed $\Re_\tau = 720$, J. Fluid Mech. **937**, A22 (2022).

[17] M. De Marchis and E. Napoli, Effects of irregular two-dimensional and three-dimensional surface roughness in turbulent channel flows, Int. J. Heat Fluid Flow **36**, 7 (2012).

[18] R. J. Volino, M. P. Schultz, and K. A. Flack, Turbulence structure in a boundary layer with two-dimensional roughness, J. Fluid Mech. **635**, 75 (2009).

[19] R. J. Hardy, J. L. Best, T. I. Marjoribanks, D. R. Parsons, and P. J. Ashworth, The influence of three-dimensional topography on turbulent flow structures over dunes in unidirectional flows, JGR Earth Surface **126**, e2021JF006121 (2021).

[20] L. Djenidi, R. A. Antonia, M. Amielh, and F. Anselmet, A turbulent boundary layer over a two-dimensional rough wall, Exp. Fluids **44**, 37 (2007).

[21] A. M. Hamed, A. Kamdar, L. Castillo, and L. P. Chamorro, Turbulent boundary layer over 2D and 3D large-scale wavy walls, Phys. Fluids **27**, 106601 (2015).

[22] A. M. Hamed, M. Sadowski, Z. Zhang, and L. P. Chamorro, Transition to turbulence over 2D and 3D periodic large-scale roughnesses, J. Fluid Mech. **804**, R6 (2016).

[23] G. Blois, K. T. Christensen, J. L. Best, G. Elliott, J. Austin, C. Dutton, M. Bragg, M. Garcia, and B. Fouke, A versatile refractive-index-matched flow facility for studies of complex flow systems across scientific disciplines, in *50th AIAA Aerospace Sciences Meeting including the New Horizons Forum and Aerospace Exposition, Nashville, Tennessee, 2012* (AIAA, Reston, VA, 2012), AIAA Paper No. 2012–0736.

[24] K. Bai and J. Katz, On the refractive index of sodium iodide solutions for index matching in PIV, Exp. Fluids **55**, 1704 (2014).

[25] L. Chan, M. MacDonald, D. Chung, N. Hutchins, and A. Ooi, A systematic investigation of roughness height and wavelength in turbulent pipe flow in the transitionally rough regime, J. Fluid Mech. **771**, 743 (2015).

[26] S. B. Pope, Turbulent flows, Meas. Sci. Technol. **12**, 2020 (2001).

[27] L. P. Chamorro, C. Hill, S. Morton, C. Ellis, R. E. A. Arndt, and F. Sotiropoulos, On the interaction between a turbulent open channel flow and an axial-flow turbine, J. Fluid Mech. **716**, 658 (2013).

[28] P. Saarenrinne and M. Piirto, Turbulent kinetic energy dissipation rate estimation from PIV velocity vector fields, Exp. Fluids **29**, S300 (2000).

[29] L. Luznik, W. Zhu, R. Gurka, J. Katz, W. N. Smith, and T. R. Osborn, Distribution of energy spectra, Reynolds stresses, turbulence production, and dissipation in a tidally driven bottom boundary layer, J. Phys. Oceanogr. **37**, 1527 (2007).

[30] J. Sheng, H. Meng, and R. O. Fox, A large eddy PIV method for turbulence dissipation rate estimation, Chem. Eng. Sci. **55**, 4423 (2000).

[31] S. Cheng, S. Kaufman, V. Tipnis, J. L. Best, and L. P. Chamorro, Effects of low clay concentrations on nearly isotropic turbulence, Phys. Rev. Fluids **7**, 073801 (2022).

[32] J. Hong, J. Katz, and M. P. Schultz, Near-wall turbulence statistics and flow structures over three-dimensional roughness in a turbulent channel flow, J. Fluid Mech. **667**, 1 (2011).

[33] P. Cherukat, Y. Na, T. J. Hanratty, and J. B. McLaughlin, Direct numerical simulation of a fully developed turbulent flow over a wavy wall, Theor. Comput. Fluid Dyn. **11**, 109 (1998).

[34] R. A. Antonia, J. Kim, and L. W. B. Browne, Some characteristics of small-scale turbulence in a turbulent duct flow, J. Fluid Mech. **233**, 369 (1991).

[35] S. S. Lu and W. W. Willmarth, Measurements of the structure of the Reynolds stress in a turbulent boundary layer, J. Fluid Mech. **60**, 481 (1973).

[36] K. P. Nolan, E. J. Walsh, and D. M. McEligot, Quadrant analysis of a transitional boundary layer subject to free-stream turbulence, J. Fluid Mech. **658**, 310 (2010).

[37] W. Yue, C. Meneveau, M. B. Parlange, W. Zhu, R. Van Hout, and J. Katz, A comparative quadrant analysis of turbulence in a plant canopy, Water Resour. Res. **43**, 2006WR005583 (2007).

[38] L. Keirsbulck, L. Labraga, A. Mazouz, and C. Tournier, Surface roughness effects on turbulent boundary layer structures, J. Fluids Eng. **124**, 127 (2002).

[39] M. P. Schultz and K. A. Flack, Outer layer similarity in fully rough turbulent boundary layers, Exp. Fluids **38**, 328 (2005).

[40] J. Finnigan, K. Ayotte, I. Harman, G. Katul, H. Oldroyd, E. Patton, D. Poggi, A. Ross, and P. Taylor, Boundary-layer flow over complex topography, Boundary-Layer Meteorol. **177**, 247 (2020).

[41] J. M. Wallace, Quadrant analysis in turbulence research: History and evolution, Annu. Rev. Fluid Mech. **48**, 131 (2016).

[42] R. J. Volino, M. P. Schultz, and K. A. Flack, Turbulence structure in boundary layers over periodic two-and three-dimensional roughness, J. Fluid Mech. **676**, 172 (2011).

[43] S. Li, Z. Zhou, X. Yang, G. He, and H. Chen, Flow statistics and similarity in rough-wall periodic hill flows, Phys. Rev. Fluids **10**, 104608 (2025).

[44] Y. Wu, H. Ren, and H. Tang, Turbulent flow over a rough backward-facing step, Int. J. Heat Fluid Flow **44**, 155 (2013).